Applied Catalysis B: Environmental 203 (2017) 494–504

Contents lists available at ScienceDirect

Applied Catalysis B: Environmental

journal homepage: www.elsevier.com/locate/apcatb

Efficient UV–vis-infrared light-driven catalytic abatement of benzene on amorphous manganese oxide supported on anatase TiO_2 nanosheet with dominant {001} facets promoted by a photothermocatalytic synergetic effect

Lan Lan, Yuanzhi Li*, Min Zeng, Mingyang Mao, Lu Ren, Yi Yang, Huihui Liu, Li Yun, Xiujian Zhao

State Key Laboratory of Silicate Materials for Architectures, Wuhan University of Technology, 122 Luoshi Road, Wuhan 430070, PR China

ARTICLE INFO

Article history:
Received 1 September 2016
Received in revised form 11 October 2016
Accepted 18 October 2016
Available online 19 October 2016

Keywords:
Anatase TiO_2 nanosheets
Manganese oxide
Nanocomposite
UV–Vis-IR photocatalysis
Photothermocatalytic
Benzene oxidation

ABSTRACT

The nanocomposites of amorphous manganese oxide (MnO_x) supported on anatase TiO_2 nanosheet with dominant {001} facets (TNS) with different Mn/Ti molar ratio were prepared by hydrothermal redox reaction of $KMnO_4$ and $Mn(NO_3)_2$ in the presence of TNS. The MnO_x/TNS nanocomposites were characterized by XRD, SEM, TEM, ICP, XPS, BET, and diffuse reflectance UV–vis-Infrared adsorption. MnO_x/TNS with the optimum Mn/Ti molar ratio of 0.40 exhibits highly efficient photothermocatalytic activity and excellent durability for the oxidation of the recalcitrant and carcinogenic benzene under the full solar spectrum irradiation from a Xe lamp. Remarkably, the CO_2 production rate of MnO_x/TNS enhances by 99 times as compared to TNS. Impressively, MnO_x/TNS also exhibits efficient photocatalytic activity with the visible-infrared irradiation, even with the infrared irradiation. The highly efficient photothermocatalytic activity of MnO_x/TNS under the full solar spectrum irradiation originates from the highly efficient solar light-driven thermocatalysis on MnO_x due to its strong absorption in entire solar spectrum region and the efficient thermocatalytic activity, which is considerably promoted by a photothermocatalytic synergetic effect. We put insight into the photothermocatalytic synergetic effect by CO temperature-programmed reduction of MnO_x/TNS in dark and with the solar light irradiation: the active species generated by the photocatalysis on TNS migrate to MnO_x via the MnO_x/TiO_2 interface, and accelerate the solar light-driven thermocatalysis on MnO_x in the nanocomposite.

1. Introduction

Anatase TiO_2 nanocrystal with dominant {0 0 1} facets has attracted enormous interests due to its unique physicochemical properties such as high surface energy, active unsaturated Ti atoms, etc., since Yang et al. reported the preparation of anatase TiO_2 single crystals with dominant {0 0 1} facets [1]. It has been widely used in photocatalytic environmental purification, photocatalytic hydrogen production, photocatalytic reduction of CO_2, selective photocatalytic synthesis of fine chemicals, dye sensitized solar cell, etc [2–7]. However, there are three major drawbacks to greatly hinder its wide photocatalytic application. The first is its low photocatalytic efficiency owing to the rapid recombination of photogenerated electron and hole. The second is its photocatalytic activation only by UV light due to its large band gap. The third is its prone deactivation due to the deposition of recalcitrant carbonaceous intermediates or the production of oxygen vacancies on the surface of TiO_2 nanosheets in the photocatalytic process [8,9]. Scientists have developed various strategies to resolve the three problems. The reported strategies of enhancing its photocatalytic efficiency involve: tuning the ratio of {001} and {101} facets of TiO_2 nanocrystals for preferential transport of photogenerated electrons and holes to different facets of the TiO_2 nanocrystals, thereby reducing the charge recombination [10–17], forming porous TiO_2 superstructure consisted of anatase TiO_2 nanocrystals with dominant {001} facets [18], forming unique anatase TiO_2 twin crystals with {001} facets [19], creating defects (e.g. oxygen vacancies) on {001} facets of anatase TiO_2 nanosheets [20,21], surface modification of TiO_2 with F to reduce the recombination rate of photo-generated electrons and holes, or enhance the adsorption of

* Corresponding author.
E-mail addresses: liyuanzhi66@hotmail.com, liyuanzhi66@hotmail.com (Y. Li).

http://dx.doi.org/10.1016/j.apcatb.2016.10.047
0926-3373/

O_2 so as to promote the photogenerated electrons captured by the adsorbed O_2 [22,23],forming nanocomposites with of grapheme [24–27], 2D-MoS_2 [28], layered Ti_3C_2[29], quantum Cu(II) nanodot [30] to retard the recombination of photogenerated charge carriers and prolong electron lifetime, and so on.

The reported strategies of extending its photocatalytic response from UV to visible region include: doping by nonmetals such as nitrogen [31], carbon [33], co-doping by nonmetal and metal [34,35], forming nanocomposites with semiconductors with narrow band gap such as CdS [36], Bi_2O_3 quantum dots [37], CdSe quantum dots [38], and g-C_3N_4 [39], forming plasmonic photocatalyst of Au/TiO_2 [40] and Au-Pd/TiO_2 nanosheets [41], utilizing the interaction between reactant and TiO_2 nanosheet to form surface complex with visible photocatalytic response [42], etc. Among the reported strategies, only the plasmonic photocatalysts of Au/TiO_2 and Au-Pd/TiO_2 were reported to exhibit very low photocatalytic activity for photocatalytic H_2 production under near-infrared irradiation above 780 nm [42]. All other strategies just extend its photocatalytic response to visible region with maximum wavelength up to ~600 nm [31–39].

The reported strategies of improving photocatalytic durability of anatase TiO_2 nanocrystal with dominant {001} facets are very limited [8,43]. Xu et al. revealed the origin of deactivation of anatase TiO_2 nanosheet with dominant {001} facets, and reported a regeneration method by simply refluxing the deactivated TiO_2 nanosheet in water at 100 °C [8]. Stefanov et al. [43] reported a method of improving its photocatalytic stability for gas-phase photodegradation of acetaldehyde by controlling reaction condition such as humidity and temperature.

Most of the published works about the anatase TiO_2 nanosheet with dominant {001} facets focused on the photocatalytic degradation of water pollutants (especially, dyes) and photocatalytic production of H_2. There have been only few works about the anatase TiO_2 nanosheet with dominant {001} facets for the photocatalytic degradation of volatile organic compounds (VOCs) [6,9,22,23,42–44], which are major components of air pollutants emitted in very large scale from various industrial processes related to the production and utilization of paints, organic chemicals, etc. To achieve the application of TiO_2 nanosheet with dominant {001} facets in the efficient abatement of VOCs using renewable solar energy, it is highly desirable but great challenging to develop a novel strategy of significantly improving its photocatalytic activity as well as durability, or/and efficiently extending its photocatalytic response from UV to visible region, even to infrared region. Very recently, we found a photothermocatalytic synergetic effect that can significantly enhance the catalytic activity and the durability of TiO_2 nanosheet with dominant {001} facets for the gas-phase abatement of benzene [45]. However, the TiO_2 nanosheet with dominant {001} facets only utilize UV light and the heating effect of infrared light for photocatalytic abatement of benzene. Herein, we prepared a novel nanocomposite of amorphous manganese oxide supported on anatase TiO_2 nanosheet with dominant {001} facet (MnO_x/TNS). By forming the MnO_x/TNS nanocomposite, both the photocatalytic activity and durability of anatase TiO_2 nanosheet with dominant {001} facet are significantly improved, and its photocatalytic response is efficiently extended from UV to whole solar spectrum region. The MnO_x/TNS nanocomposite exhibits highly efficient photothermocatalytic activity for the oxidation of the recalcitrant and carcinogenic benzene under the full solar spectrum, visible-infrared, or infrared irradiation. Remarkably, the CO_2 production rate of the MnO_x/TNS nanocomposite enhances by 99 times as compared to the pure TiO_2 nanosheet. The highly efficient photothermocatalytic activity of the MnO_x/TNS nanocomposite under the full solar spectrum irradiation is attributed to the highly efficient solar light-driven thermocatalysis on the amorphous manganese oxide considerably promoted by a photothermocatalytic synergetic effect. We put insight into the solar light-driven thermocatalysis and the photothermocatalytic synergetic effect.

2. Experimental section

2.1. Preparation

Anatase TiO_2 nanosheet with dominant {001} facets, denoted as TNS, was prepared by a hydrothermal reaction of $Ti(OBu)_4$ in the presence of HF at 180 °C according to the procedure reported in our previous work.[42] The BET surface area of the anatase TiO_2 nanosheet is 95.7 $m^2 g^{-1}$. The percentage of the dominant {001} facets is estimated by the average thickness and length to be 72.3% [42].

The MnO_2/TiO_2 composites were prepared according to the following procedure. 1.0 g of anatase TiO_2 nanosheet was added into 50 mL of distilled water in a beaker, then ultrasonicated for 60 min until it was well dispersed. 0.1319 g of $KMnO_4$ and 0.1494 g of $Mn(NO_3)_2$ (50 wt%) solution with a $KMnO_4/Mn(NO_3)_2$ molar ratio of 2:1 were added into the suspension, and ultrasonicated for 10 min until they were dissolved. The beaker was covered with polyethylene film, and then placed into an electrical oven at 90 °C for 12 h. The precipitate formed in the solution was filtered, washed with distilled water, and dried in the electrical oven at 90 °C for 12 h. The obtained MnO_x/TiO_2 sample with the Mn/Ti molar ratio of 0.10 is denoted as MnO_x/TNS-A.

The MnO_x/TiO_2 samples with higher Mn/Ti molar ratio of 0.20, 0.40, and 0.60 were prepared by the same procedure as MnO_x/TNS-A except for adding the higher amount of $KMnO_4$ and $Mn(NO_3)_2$ (50 wt%) according to the same $KMnO_4/Mn(NO_3)_2$ molar ratio of 2:1. The obtained MnO_x/TiO_2 samples were denoted as MnO_x/TNS-B, MnO_x/TNS-C, and MnO_x/TNS-D, respectively.

The pure manganese oxide sample was prepared by the same procedure as MnO_x/TNS-A except for no adding TiO_2 nanosheet.

2.2. Characterization

The X-ray diffraction (XRD) patterns of the samples were obtained on a Rigaku Dmax X-ray diffractometer using Cu Ka radiation. SEM image and energy dispersive X-ray spectroscopy (EDX) mapping of elements were obtained on an ULTRA PLUS-43-13 scanning electron microscope. The chemical composition of the samples was analyzed by inductively coupled plasma/optical emission spectroscopy (ICP-OES, PerkinElmer Optima 4300DV). Transmission electron microscopy (TEM) images were observed on a JEM-100CX electron microscope. Diffusive reflectance UV–vis-IR (DRUV-Vis-IR) absorption spectra were recorded on a UV-3600 spectrophotometer. X-ray photoelectron spectroscopy (XPS) measurement was performed on a VG Multilab 2000 X-ray photoelectron spectrometer using Mg Ka radiation. BET surface area was measured on an ASAP2020 using N_2 adsorption at −196 °C.

CO temperature programmed reduction (CO-TPR) of the MnO_x/TNS-C sample in dark or with irradiation was measured in a quartz tube reactor on TP-5080 multifunctional adsorption apparatus equipped with a TCD detector. A quartz window was connected to one of the end of the quartz tube reactor. A Xe lamp (CHF-XM500), which has a spectral profile similar to the solar spectrum,[46] was put in the front of the quartz window. For measured the CO-TPR of the MnO_x/TNS-C sample under the irradiation with wavelength above 480 nm, a long wave pass cutoff filter of 480 nm was placed between the Xe lamp and the quartz window. The detailed procedure was reported in our previous work [47,48].

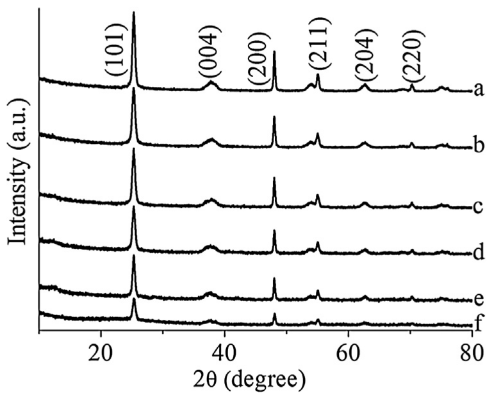

Fig. 1. XRD patterns of TNS (a), MnO_x/TNS-A (b), MnO_x/TNS-B (c), MnO_x/TNS-C (d), MnO_x/TNS-D (e), and the sample of MnO_x/TNS-C after the recycled catalytic test (f).

2.3. Photothermocatalytic activity

The phtotothermocatalytic activity of the samples for benzene oxidation under the irradiation of the Xe lamp was measured in a closed cylindrical stainless steel gas-phase reactor with a quartz window, which was connected to a gas chromatograph (GC9560) to analyze the reactants and products. The experimental set-up and detailed procedure were described in our previous work [46,47]. To measure the photothermocatalytic activity of the samples under the irradiation of visible-infrared or infrared light from the Xe lamp, a long wave pass cutoff filter of 420, 480, 560, 690 or 830 nm, was put in front of the quartz window of the reactor. The light intensity of the full solar spectrum, visible-infrared or infrared light above 420, 480, 560, 690, and 830 nm is 412.9, 383.7, 356.4, 335.5, 287.1, 238.8 mW cm^{-2}, respectively.

The recycled tests of benzene oxidation on the MnO_x/TNS-F sample under the irradiation of the Xe lamp were performed according to the procedure reported in our previous works [46,49]. The reaction time of each catalytic test cycle was 30 min, and the procedure was repeated 30 times.

2.4. Photocatalytic activity

The photocatalytic activity of the MnO_x/TNS-C sample for benzene oxidation at room temperature under the irradiation of the Xe lamp was measured in the closed cylindrical stainless steel gas-phase reactor with a quartz window according to the procedure reported in our previous work[49,50].

2.5. Thermocatalytic activity

The thermocatalytic activity of the samples for benzene oxidation was measured in a continuous flow fixed-bed quartz tubular reactor on an online gas-phase reaction apparatus (WFS-2015) at different temperature in dark. The detailed procedure was described in our previous work [51,52]. The reaction condition is as follows: benzene concentration is 2.0 g m^{-3}, space velocity (SV) = 48000 mL $g_{catalyst}{}^{-1}$ h^{-1}.

2.6. The catalytic activity at the different temperature in the dark or with the irradiation

The thermocatalytic activity of the MnO_x/TNS-C sample for benzene oxidation at the different temperature in the dark or with the irradiation of the Xe lamp was measured in a flow fixed quartz tube reactor on a WFS-2015 online gas-phase reaction apparatus. A quartz window was connected to one of the end of the quartz tube reactor. The detailed procedure was described in our previous work [48]. The reaction condition is as follows: benzene concentration is 2.0 g m^{-3}, space velocity (SV) = 96000 mL $g_{catalyst}{}^{-1}$ h^{-1}.

3. Results and discussion

3.1. Characterization

The MnO_x/TiO_2 nanocomposites with different Mn/Ti molar ratio of 0.10, 0.20, 0.40, and 0.600 were prepared by hydrothermal redox reaction of $KMnO_4$ and $Mn(NO_3)_2$ with $KMnO_4/Mn(NO_3)_2$ molar ratio of 2:1 in the presence of anatase TiO_2 nanosheet with dominant {001} facets (TNS) at 90 °C. The corresponding MnO_x/TiO_2 nanocomposites are denoted as MnO_x/TNS-A, MnO_x/TNS-B, MnO_x/TNS-C, and MnO_x/TNS-D, respectively. The XRD analysis shows that all the samples of MnO_x/TNS nanocomposites have the same XRD patterns as that of the TiO_2 nanosheet with pure anatase structure (PDF 04-0477), and no XRD patterns of manganese oxide are observed (Fig. 1). This result indicates that manganese oxide supported on the anatase TiO_2 nanosheet for the all MnO_x/TiO_2 nanocomposites is amorphous.

Fig. 2 shows SEM images with EDX element mapping for MnO_x/TNS-C. As shown in Fig. 2, Mn is uniformly distributed on TiO_2 nanosheets, and no segregated manganese oxide is observed. Similar phenomena are observed for MnO_x/TNS-A and MnO_x/TNS-B (Fig. S1 and S2 , Supporting information). For MnO_x/TNS-D with higher Mn/Ti molar ratio (0.600), most of Mn is uniformly distributed on TiO_2 nanosheet while a small amount of manganese oxide nanorods are observed (Fig. S3). The Mn/Ti molar ratio of the MnO_x/TNS nanocomposites is measured by ICP-OES (Table 1). The molar ratio of MnO_x/TNS-A, MnO_x/TNS-B, MnO_x/TNS-C, and MnO_x/TNS-D is 0.12, 0.24, 0.48, 0.70, respectively, which is in general agreement to the corresponding data in the reactants.

Fig. 3 shows TEM images of the MnO_x/TNS composites. For MnO_x/TNS-A, MnO_x/TNS-B, and MnO_x/TNS-C, only nanosheets are observed (Fig. 3A-3C). Some nanosheets lie flat on the TEM grid while other nanosheets stand vertically on the TEM grid. HRTEM indicates that TiO_2 nanosheet has dominant {001} facets. A portion of TiO_2 nanosheet surface is obscured and no crystalline manganese oxide is observed (Fig. 4A–C, pointed by dotted circle). The HRTEM observation together with the result of XRD as well as EDX element mapping reveals that amorphous manganese oxide is grown on the surface of TiO_2 nanosheets. For MnO_x/TNS-D with higher Mn/Ti molar ratio (0.600), most surface area of TiO_2 nanosheet becomes obscure (Fig. 3D and 4D), suggesting that amorphous manganese oxide is grown on TiO_2 nanosheets. In addition, several nanorods are observed (Fig. 3D). HRTEM reveals that a selected nanorod is cryptomelane-type octahedral molecular sieve (OMS-2) with 0.49 nm lattice spacing of {200} facet (Fig. 4F) [51]. The amount of OMS-2 nanorods in MnO_x/TNS-D is quite low because OMS-2 is not detected by XRD. HRTEM indicates that no crystalline manganese oxide is observed on the obscured surface of TiO_2 nanosheet (Fig. 4D), suggesting that manganese oxide on the surface of TiO_2 nanosheet for MnO_x/TNS-D is amorphous.

The specific area of the samples was measured by N_2 adsorption. Compared to the BET surface area of the pure TiO_2 nanosheet (TNS, 95.7 m^2 g^{-1}), the formation of the MnO_x/TNS nanocomposites leads to an increase in the BET surface area. With the increase of Mn/Ti molar ratio, the BET surface of the MnO_x/TNS nanocomposites increases. The BET surface area of MnO_x/TNS-A, MnO_x/TNS-B, MnO_x/TNS-C, and MnO_x/TNS-D is 104.0, 141.6, 144.2, 159.0 m^2 g^{-1} (Table 1), respectively.

The oxidation state of Mn in the MnO_x/TNS nanocomposites is analyzed by XPS spectra of $Mn2p_{3/2}$. As shown in Fig. 5A, the $Mn2p_{3/2}$ spectra are fitted by two peaks around 641.8 eV and 643.6 eV. The peak around 641.8 eV is assigned to the

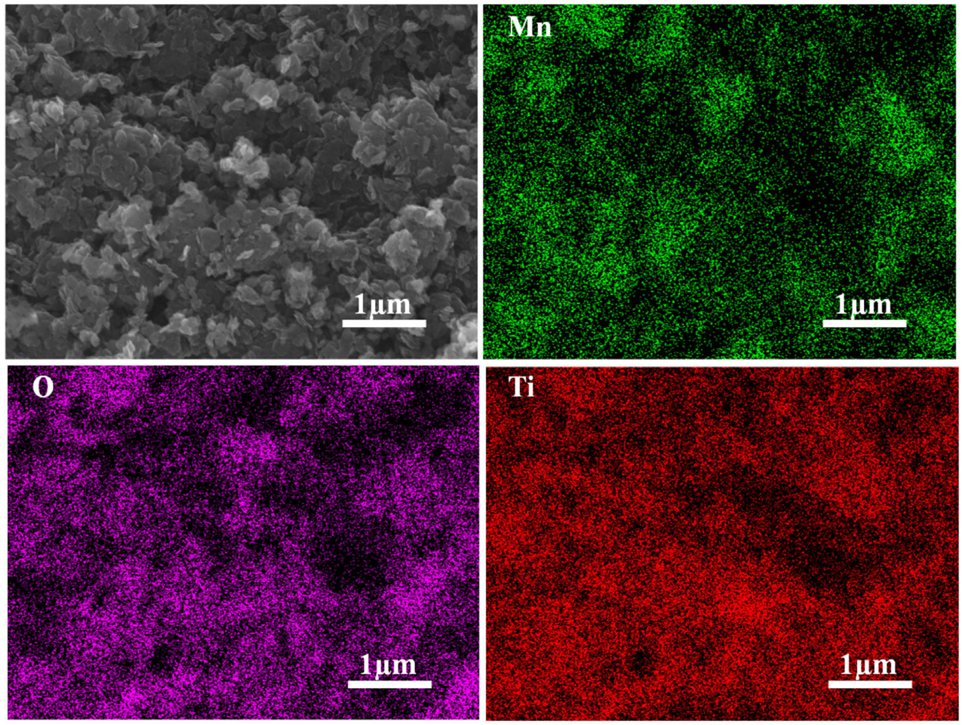

Fig. 2. SEM images with EDX element mapping for MnO_x/TNS-C.

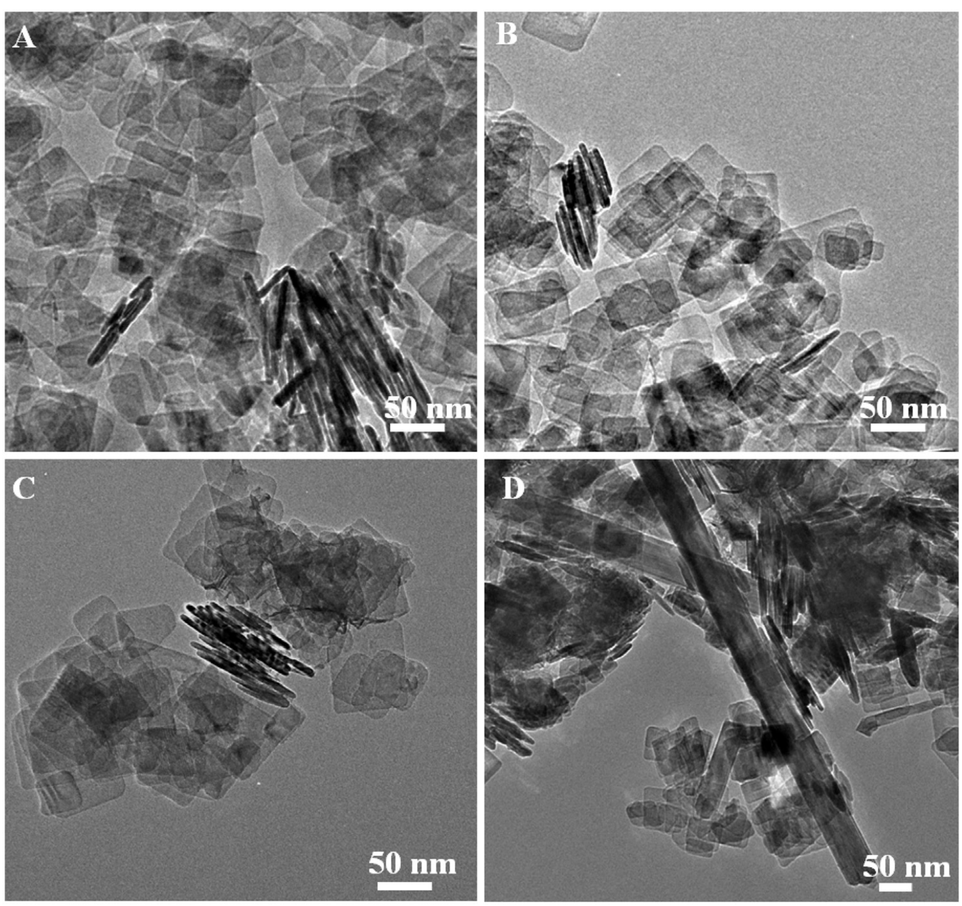

Fig. 3. TEM images of MnO_x/TNS-F-A (A), MnO_x/TNS-F-B (B), MnO_x/TNS-F-C (C) and MnO_x/TNS-F-D (D).

Table 1
Mn/Ti molar ratio in reactants, Mn/Ti molar ratio measured by ICP, Mn^{3+}/Mn^{4+} molar ratio measured by XPS, and BET surface area of the samples.

Sample	Mn/Ti molar ratio in reactants	Mn/Ti molar ratio by ICP	Mn^{3+}/Mn^{4+} molar ratio by XPS	BET surface area (m^2 $g-^1$
TNS				95.7
MnO_x/TNS-A	0.10	0.12	10.00	104.0
MnO_x/TNS-B	0.20	0.24	4.45	141.6
MnO_x/TNS-C	0.40	0.48	2.70	144.2
MnO_x/TNS-D	0.60	0.70	1.58	159.0

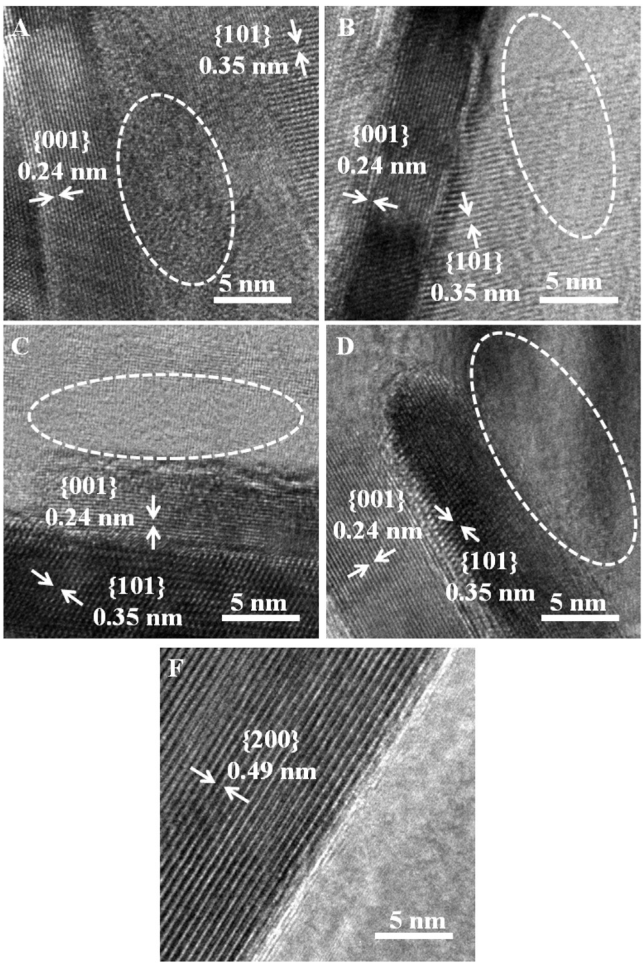

Fig. 4. HRTEM images of the nanosheet for MnO_x/TNS-A (A), MnO_x/TNS-B (B), MnO_x/TNS-C (C), MnO_x/TNS-D (D), and nanorod for MnO_x/TNS-D (E): lattice spacing of 0.35 nm is corresponding to {101} facet of anatase TiO_2.

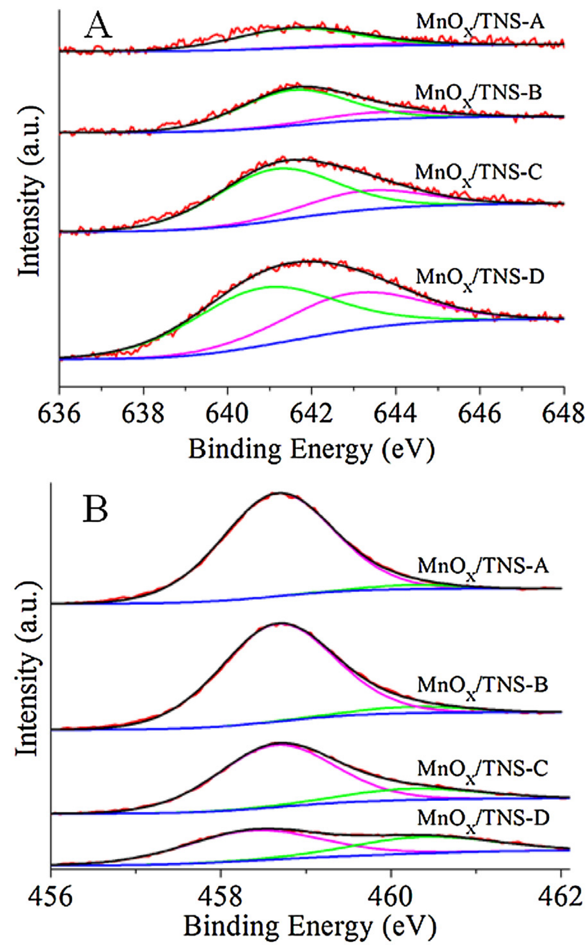

Fig. 5. XPS spectra of Mn $2p_{3/2}$ (A) and Ti $2p_{3/2}$ (B).

Mn^{3+} while the peak around 643.6 eV is assigned to the Mn^{4+} [51,52]. No other Mn species (e.g. Mn^{2+}) is detected by XPS. The MnO_x/TNS-A with lower Mn/Ti molar ratio (0.10) has high Mn^{3+}/Mn^{4+} molar ratio of 10.0, indicating that amorphous manganese oxide on the surface of TiO_2 nanosheets mainly exist in the form of Mn^{3+}. With the elevation of the Mn/Ti molar ratio, the Mn^{3+}/Mn^{4+} molar ratio considerably decreases. Compared to MnO_x/TNS-A, the Mn^{3+}/Mn^{4+} molar ratio of MnO_x/TNS-B, MnO_x/TNS-C, and MnO_x/TNS-D decreases from 10.0 to 4.45, 2.70, and 1.58, respectively (Table 1). According to the Mn^{3+}/Mn^{4+} molar ratio, the formula of MnO_x/TNS-A, MnO_x/TNS-B, MnO_x/TNS-C, and MnO_x/TNS-D is determined to be $MnO_{1.55}/TiO_2$, $MnO_{1.59}/TiO_2$, $MnO_{1.64}/TiO_2$, and $MnO_{1.69}/TiO_2$, respectively.

The oxidation state of Ti in the MnO_x/TNS nanocomposites is analyzed by XPS spectra of $Ti2p_{3/2}$. As shown in Fig. 5B, the $Ti2p_{3/2}$ spectra of the MnO_x/TNS nanocomposites are fitted by a strong peak around 458.4 eV and shoulder peak around 460.5 eV. The strong peak around 458.4 eV is assigned to Ti^{4+} in bulk TiO_2 [22,53]. With the increase of Mn/Ti molar ratio, the shoulder peak around 460.5 eV is intensified. Therefore, the peak around 460.5 eV is attributed to Ti^{4+} in the interface of MnO_x/TiO_2 for the MnO_x/TNS nanocomposites. The higher binding energy of Ti^{4+} in the interface of MnO_x/TiO_2 as compared to that of Ti^{4+} in bulk TiO_2 reveals the existence of a strong interaction between MnO_x and TiO_2. As the dominant {001} facets of anatase TiO_2 nanosheet have active unsaturated Ti atoms (five coordinated) [1], –Mn–O–Ti– bonds are easily formed at the unsaturated Ti atoms to stabilize the high surface-energy {001} facets during the growth of manganese oxide on the surface of TiO_2 nanosheet (Fig. 2-4). As the ionization potential of Mn is higher than that of Ti [54], the binding energy of Ti^{4+} in the interface of MnO_x/TiO_2 is enhanced.

3.2. Photothermocatalytic activity

The photothermocatalytic activity of the MnO_x/TNS nanocomposites was measured by evaluating CO_2 production rate from the gas-phase oxidation of the recalcitrant and carcinogenic benzene

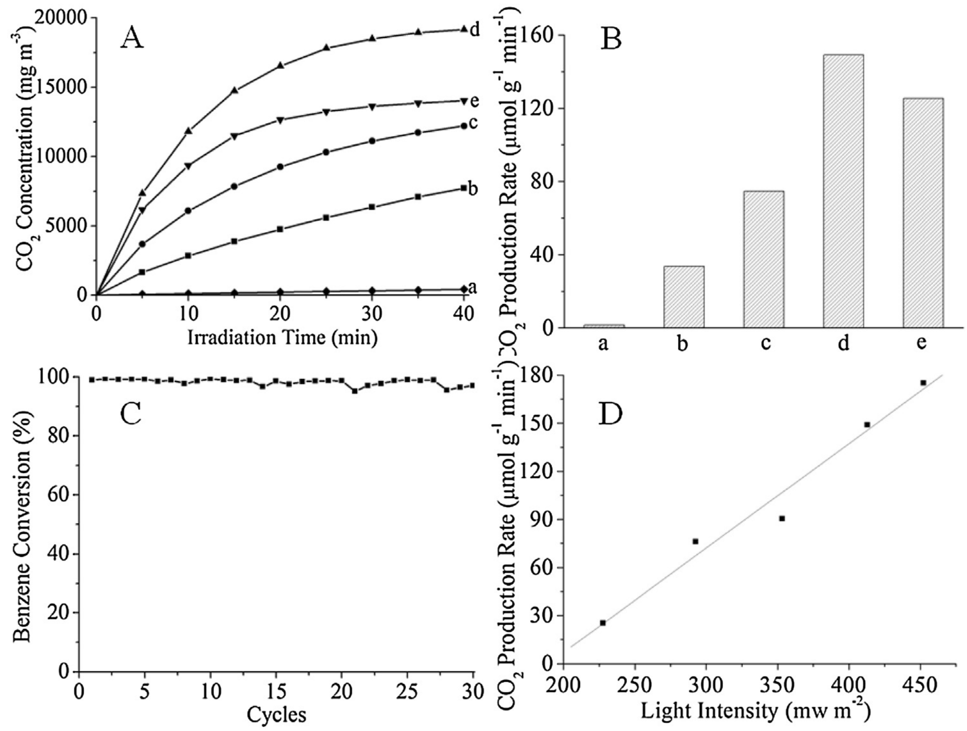

Fig. 6. Time course of CO_2 produced from benzene oxidation (A); r_{CO_2} for benzene oxidation on catalysts (B); the durability of MnO_x/TNS-C for benzene oxidation under the irradiation of Xe lamp (C); the r_{CO_2} of benzene oxidation of MnO_x/TNS-C under the irradiation of the Xe lamp with different light intensity: TNS (a), MnO_x/TNS-A (b), MnO_x/TNS-B (c), MnO_x/TNS-C (d), and MnO_x/TNS-D (e).

(one of typical VOCs) under the irradiation of a Xe lamp. As shown in Fig. 6A, the pure TiO_2 nanosheet (TNS) exhibits a very low photocatalytic activity. After the irradiation of full solar spectrum for 40 min, the concentration of CO_2 produced is 423.4 mg m^{-3}. The initial CO_2 production rate (r_{CO2}) of TNS, defined as the amount of CO_2 produced per gram of catalyst per unit time in the initial five minutes, is only 1.50 μmol g^{-1} min^{-1} (Fig. 6B). Loading a small amount of amorphous manganese oxide on TNS (Mn/Ti molar ratio = 0.10) leads to a significant enhancement in photothermocatalytic activity. After the irradiation of Xe lamp for 40 min, the concentration of CO_2 produced is 7705.6 mg m^{-3}. The r_{CO2} MnO_x/TNS-A is 33.6 μmol g^{-1} min^{-1}, enhanced by 22.4 times as compared to TNS. Increasing the Mn/Ti molar ratio results in an obvious enhancement in photothermocatalytic activity. With the elevation of the Mn/Ti molar ratio from 0.10 to 0.20 (MnO_x/TNS-B), the r_{CO2} increases to 74.6 μmol g^{-1} min^{-1}. When the Mn/Ti molar ratio increases to 0.40, the photothermocatalytic activity of MnO_x/TNS-C reaches the maximum. After the irradiation for 40 min, the concentration of CO_2 increases to 19162.7 mg m^{-3}. The r_{CO2} of MnO_x/TNS-C is as high as 149.0 μmol g^{-1} min^{-1}, enhanced by 99.0 times as compared to TNS. When the Mn/Ti molar ratio further increases to 0.600 (MnO_x/TNS-D), there is a slight decrease in photothermocatalytic activity. The r_{CO2} of MnO_x/TNS-C reduces to 125.3 μmol g^{-1} min^{-1} (Fig. 6B).

The catalytic durability of MnO_x/TNS-C for benzene oxidation under the irradiation of the Xe lamp was measured (Fig. 6C). At the first cycle of the catalytic test which takes 30 min, benzene conversion is 98.9%. When the sample of MnO_x/TNS-C is recycled for 30 times, the photothermocatalytic activity of MnO_x/TNS-C maintains unaltered. The result demonstrates that the MnO_x/TNS-C nanocomposite exhibits excellent catalytic durability. After the durability test, the used sample of MnO_x/TNS-C was characterized by XRD and TEM. No crystalline manganese oxide is observed by XRD (Fig. 1e) and HRTEM (Fig. S4). The result indicates that the manganese oxide supported on the surface of TiO_2 nanosheets in the used sample of MnO_x/TNS-C remains amorphous as the fresh sample of MnO_x/TNS-C.

The photothermocatalytic activity of MnO_x/TNS-C for benzene oxidation under the full solar spectrum irradiation with different light intensity was measured. At the light intensity of 227.5 mW cm^{-2}, its r_{CO_2} is 25.4 μmol g^{-1}. Increasing the light intensity results in a significant enhancement in the photothermocatalytic activity. With the elevation of the light intensity from 227.5 to 292.5, 353.1, 412.9, 452.3 mW cm^{-2}, its r_{CO_2} considerably increases from 25.4 to 76.1, 90.5, 149.0, 175.2 μmol g^{-1} min^{-1}, respectively.

To confirm whether the MnO_x/TNS nanocomposites exhibit visible and infrared photothermocatalytic activity, we evaluated the photothermocatalytic activity of MnO_x/TNS-C for benzene oxidation under the irradiation with wavelength above 420, 480, 560, 690, or 830 nm by using the corresponding cutoff filters. As shown in

Fig. 7, MnO_x/TNS-C exhibits efficient photothermocatalytic activity under the visible-infrared irradiation. The r_{CO_2} of MnO_x/TNS-C under the visible-infrared irradiation above 420, 480, 560, or 690 nm is 109.8, 90.7, 90.7, 74.2 μmol g^{-1} min^{-1}, respectively. Even under the infrared irradiation above 830 nm, MnO_x/TNS-C exhibits photothermocatalytic activity for benzene oxidation with the r_{CO_2} of 17.3 μmol g^{-1} min^{-1}. The considerable reduction in the infrared photothermocatalytic activity as compared to that with visible-infrared irradiation above 420 nm is ascribed to the reduction in the infrared light intensity. To confirm this explanation, the photothermocatalytic activity of MnO_x/TNS-C for benzene oxidation under the infrared irradiation above 830 nm with higher light intensity was measured. With the elevation of infrared light intensity from 238.8 to 265.6 mW cm^{-2}, the r_{CO_2} of MnO_x/TNS-C considerably enhances to 54.0 μmol g^{-1} min^{-1} (Fig. 7B, HLI).

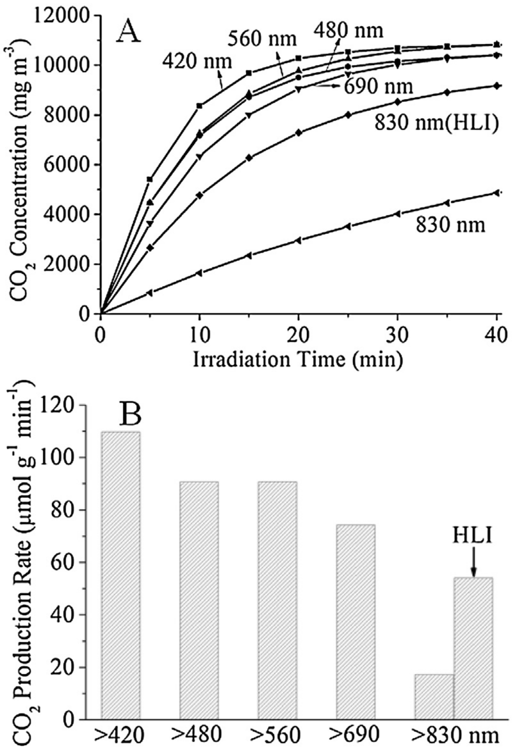

Fig. 7. Time course of CO_2 (A) and r_{CO_2} (B) for benzene oxidation on MnO_x/TNS-C under the visible-infrared or infrared irradiation from the Xe lamp by using different cutoff filters.

3.3. Mechanism

3.3.1. Photocatalysis

Why does the MnO_x/TNS nanocomposite exhibit photothermocatalytic activity with very high efficiency under the full solar spectrum, visible-infrared, or infrared irradiation, and exhibit photocatalytic activity significantly higher than the pure TiO_2 nanosheet (TNS)? As optical absorption is the prerequisite of a catalyst with photocatalytic activity under the irradiation, we measured the UV–vis-IR spectra of the samples. As shown in Fig. 8A, compared to the pure TiO_2 nanosheet (TNS), the formation of the MnO_x/TNS nanocomposites leads to a strong absorption in visible-infrared region. The MnO_x/TNS nanocomposites have strong absorption in whole solar spectrum region from 200 to 2400 nm. Increasing the Mn/TiO_2 molar ratio leads to an enhancement in the absorption. Due to the strong absorption, the highly efficient photothermocatalytic activity of the MnO_x/TNS nanocomposites under the solar light irradiation may arise from the conventional photocatalysis [55–57] and/or solar light driven thermocatalysis [46–50,58]. In order to clarify the issue, we measured the photocatalytic activity of MnO_x/TNS-C for benzene oxidation under the irradiation of the Xe lamp at ambient temperature (see Experimental). As shown in Fig. 8B, the photocatalytic activity of MnO_x/TNS-C at ambient temperature is quite low. Its photocatalytic r_{CO_2} of MnO_x/TNS-C is only 2.03 $\mu mol\,g^{-1}\,min^{-1}$, which is 73.4 times lower than the photothermocatalytic r_{CO_2} under the irradiation of the Xe lamp with the same light intensity (Fig. 8C). This result reveals that the solar light driven thermocatalysis plays a crucial role: The MnO_x/TNS nanocomposites absorb the solar engergy, and transform the absorbed solar energy to thermal energy, leading to an increase in the temperature of the MnO_x/TNS nanocomposites. When the temperature reaches the light-off temperature ($T_{light\text{-}off}$) of the thermocatalytic oxidation on the MnO_x/TNS nanocomposites, the thermocatalytic reaction starts (discussed later, Fig. 9) [46–50,58].

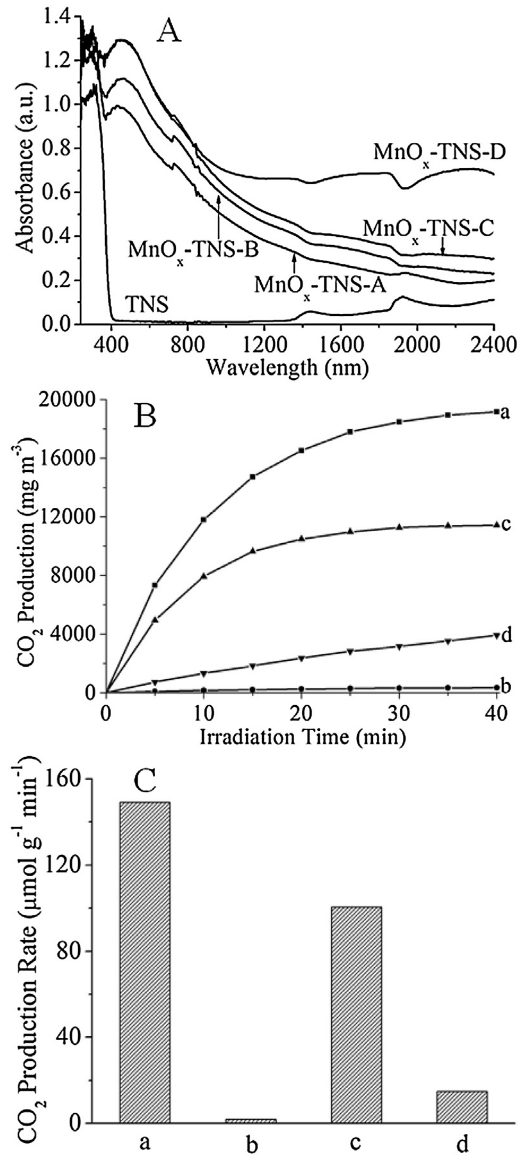

Fig. 8. Diffuse reflectance UV–vis-IR absorption of the samples (A); time course of CO_2 concentration (B) and the r_{CO_2} (C) for benzene oxidation in the different cases: on MnO_x/TNS-C under the irradiation of the Xe lamp (a) or under the irradiation of the Xe lamp at the near room temperature (b) or under the irradiation above 480 nm with higher light intensity (c), on a mechanic mixture of pure manganese oxide and pure TiO_2 nanosheet with the same Mn/Ti molar ratio as MnO_x/TNS-C (0.40) under the irradiation of the Xe lamp (d).

3.3.2. Photothermal conversion

To confirm the existence of the solar light-driven thermocatalysis, we measured the surface temperature of the MnO_x/TNS nanocomposites with the irradiation of the Xe lamp under the reaction conditions as shown in Fig. 6A. Upon the absorption of solar energy, the temperature of the MnO_x/TNS-C nanocomposite quickly increases to an equilibrium temperature (T_{eq}) owing to the photothermal conversion (Fig. 9A), at which the solar energy absorption of the MnO_x/TNS-C nanocomposite establishes equilibrium with the energy dissipation from the nanocomposite to the surroundings. The T_{eq} of MnO_x/TNS-A, MnO_x/TNS-B, MnO_x/TNS-C, and MnO_x/TNS-D is 246, 247, 250, 255 °C, respectively (Fig. 9B). The slight increase of T_{eq} with the elevation of the Mn/Ti molar ratio for the nanocomposites is attributed to the increase of the absorption in the whole solar spectrum region (Fig. 8A). The T_{eq} of MnO_x/TNS-C with the visible-infrared or infrared irradiation from

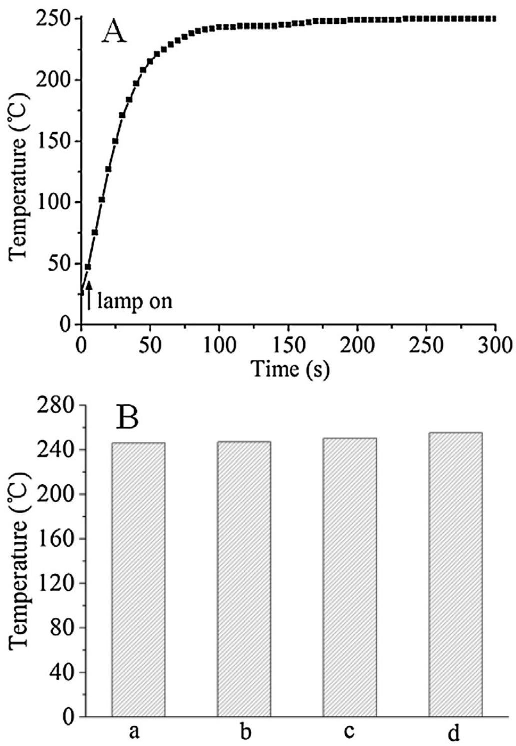

Fig. 9. Temporal temperature evolution of the MnO_x/TNS-C sample with the irradiation of the Xe lamp (A), and the equilibrium temperature of the samples with the irradiation of the Xe lamp (B): MnO_x/TNS-A (a), MnO_x/TNS-B (b), MnO_x/TNS-C (c), and MnO_x/TNS-D (d).

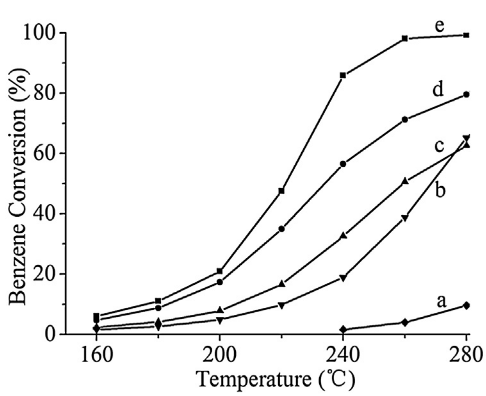

Fig. 10. Thermocatalytic activity of the samples for benzene oxidation at the different temperature in dark under the condition of benzene concentration = 2.0 g m^{-3}, space velocity (SV) = 48000 mL $g_{catalyst}^{-1}$ h^{-1}: TNS (a), MnO_x/TNS-A (b), MnO_x/TNS-B (c), MnO_x/TNS-C (d), and MnO_x/TNS-D (e).

the Xe lamp under the reaction conditions as shown in Fig. 7A was also measured. The T_{eq} of MnO_x/TNS-C with visible-infrared or infrared irradiation above 420, 480, 560, 690, and 830 nm is 247, 243, 241, 238, 185 °C, respectively (Fig. S5).

3.3.3. Thermocatalysis

To confirm whether the T_{eq} of the MnO_x/TNS nanocomposites with the solar light irradiation can reaches their corresponding $T_{light\text{-}off}$, the thermocatalytic activity of the MnO_x/TNS nanocomposites for benzene oxidation at the different temperature in dark was measured (Experimental). As shown in Fig. 10, the thermocatalytic activity of the pure TiO_2 nanosheet (TNS) is very low. When the reaction temperature increases above 240 °C, benzene starts to be oxidized on TNS ($T_{light\text{-}off}$ = ∼240 °C). Loading amorphous manganese oxide on TNS leads to a considerable improvement in thermocatalytic activity. With the elevation of the Mn/Ti molar ratio, the thermocatalytic activity of the MnO_x/TNS nanocomposites considerably increases. For all the MnO_x/TNS nanocomposites, when the reaction temperature increases above ∼160 °C, benzene starts to be oxidized ($T_{light\text{-}off}$ = ∼160 °C). All T_{eq} of the MnO_x/TNS nanocomposites with the irradiation of the Xe lamp (Fig. 9B) is higher than their corresponding $T_{light\text{-}off}$, so the solar light-driven thermocatalysis reaction on the MnO_x/TNS nanocomposites can take place. All T_{eq} of MnO_x/TNS-C with the visible-infrared or infrared irradiation (Fig. S5) is higher than its $T_{light\text{-}off}$, so the solar light-driven thermocatalysis reaction on MnO_x/TNS-C can take place.

3.4. Synergetic Effect

Do the photocatalysis on TiO_2 nanosheet and the solar light-driven thermocatalysis on the amorphous manganese oxide occur independently for benzene oxidation on the MnO_x/TNS nanocomposite under the full solar light irradiation as shown in Fig. 6? To clarify the issue, we measured the photothermocatalytic activity of MnO_x/TNS-C for benzene oxidation under the visible-infrared irradiation above 480 nm at the same temperature as the photothermocatalytic oxidation (250 °C, Fig. 9 B (c)) by increasing the visible-infrared light intensity (365.5 mW cm^{-2}). In this case, there is only the solar light driven thermocatalysis on the MnO_x/TNS-C nanocomposite, and the photocatalysis on TiO_2 nanosheet (TNS) could not proceed because anatase TiO_2 nanosheet could not be excited by the visible irradiation above 480 nm due to its large band gap (Fig. 8A). As shown in Fig. 8C, the solar light-driven thermocatalytic $r_{CO_2\text{-tc}}$ of MnO_x/TNS-C is 100.5 μmol g^{-1} min^{-1}. The photothermocatalytic $r_{CO_2\text{-ptc}}$ of MnO_x/TNS-C under the full solar spectrum irradiation (149.0 μmol g^{-1} min^{-1}) is 1.45 times higher than the summation of the photocatalytic $r_{CO_2\text{-pc}}$ of MnO_x/TNS-C (2.03 μmol g^{-1} min^{-1}) at ambient temperature and the solar light-driven thermocatalytic $r_{CO_2\text{-tc}}$ of MnO_x/TNS-C (100.5 μmol g^{-1} min^{-1}) under visible irradiation above 480 nm at the same temperature. This result indicates the existence of a synergetic effect of the photocatalysis on TiO_2 nanosheet and the solar light driven thermocatalysis on the MnO_x/TNS-C nanocomposite under the irradiation of the Xe lamp as schematically illustrated in Scheme 1:

Upon the absorption of UV light from the Xe lamp, electron in the valence band of anatase TiO_2 nanosheet is excited to the conduction band. The photogenerated hole and electron transport to the surface of anatase TiO_2 nanosheet. The photogenerated hole reacts with electron donor such as hydroxyl group, benzene to form hydroxyl radical (OH·) and active benzene ($C_6H_6^+$) because of its higher redox potential (3.02 V vs NHE) than that of hydroxyl group (e.g., OH·/OH$^-$, 1.89 V vs NHE) [55,59,60] and benzene (2.995 V vs NHE) [47]. The photogenerated electron reacts with electron acceptor (e.g. O_2) to form active oxygen species (e.g. O_2^-) due to its lower redox potential (−0.18 V vs NHE at pH = 1) than that of O_2 (O_2/O_2^-, −0.16 V vs NHE) [47,55,61].

At the same time, the solar light-driven thermocatalysis occurs on the amorphous manganese oxide. The thermocatalytic oxidation on manganese oxide follows the widely accepted Mars−van Krevelen mechanism: manganese oxide is reduced by reducible molecule (e.g. benzene), and the reduced manganese oxide is subsequently re-oxidized by gas phase oxygen [51,52]. The active species produced by photocatalysis on TiO_2 nanosheet migrate to amorphous manganese oxide via the interface of MnO_x/TiO_2. The active benzene ($C_6H_6^+$) is more active than benzene (C_6H_6) according to the molecule orbital theory as the number of electrons in the binding molecular orbital of $C_6H_6^+$ is less than that of C_6H_6 [54], thus accelerating the reduction of amorphous manganese oxide. The active oxygen species of hydroxyl radical (OH·) and O_2^-, which are

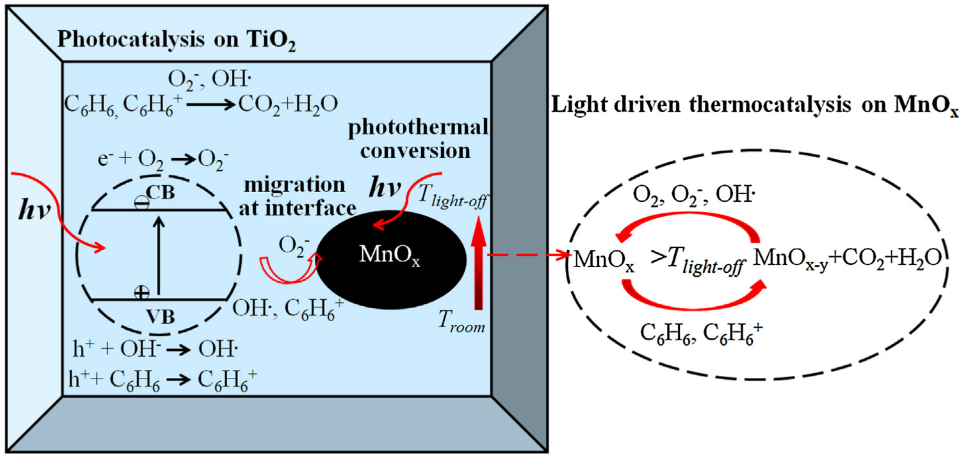

Scheme 1. Schematical illustration of the synergetic effect between the photocatalysis on anatase TiO_2 nanosheet and the solar light driven thermocatalysis on amorphous manganese oxide for the MnO_x/TiO_2 nanocomposite.

more active than O_2, accelerate the oxidation of the reduced amorphous manganese oxide. Therefore, the synergetic effect between the photocatalysis on TiO_2 nanosheet and the light-driven thermocatalysis on amorphous manganese oxide considerably enhances the photothermocatalytic activity of the MnO_x/TNS nanocomposites under the full solar spectrum irradiation.

To clarify the role of the migration of the photogenerated active species via the of MnO_x/TiO_2 interface in the photothermocatalytic synergetic effect, we measured the photothermocatalytic activity of a mechanical mixture of the pure TiO_2 nanosheet (TNS) and the pure manganese oxide with the same Mn/Ti molar ratio as MnO_x/TNS-C (0.40) for benzene oxidation under the irradiation of the Xe lamp. The pure manganese oxide, which was prepared by the same procedure as that of MnO_x/TNS-C except for the absence of the pure TiO_2 nanosheet (TNS) [51] (Experimental), has OMS-2 crystalline structure [51] with BET surface area of 61.2 $m^2\,g^{-1}$. The photothermocatalytic $r_{CO_2\text{-ptc}}$ of the mechanical mixture is 14.84 μmol g^{-1} min^{-1}, which is 10.0 times lower than the photothermocatalytic $r_{CO_2\text{-ptc}}$ of the MnO_x/TNS-C nanocomposite (149.0 μmol g^{-1} min^{-1}). The $r_{CO_2\text{-ptc}}$ of the mechanical mixture (14.84 μmol g^{-1} min^{-1}) is the almost same as the summation of the $r_{CO_2\text{-ptc}}$ of TNS and the $r_{CO_2\text{-ptc}}$ of the pure manganese oxide calculated according to the Mn/Ti molar ratio (0.40) in the mechanical mixture (14.92 g^{-1} min^{-1}). The result indicates that there is no photothermocatalytic synergetic effect in the mechanical mixture. This is easily understood as the manganese oxide is loosely contacted to the TiO_2 nanosheet in the mechanical mixture, thus the photogenerated active species on the TiO_2 nanosheet could not efficiently migrate from TiO_2 to manganese oxide. This result clearly reveals that the photothermocatalytic synergetic effect occurs at the closely contacted interface of amorphous manganese oxide/TiO_2 nanosheet in the MnO_x/TNS-C nanocomposite.

To provide more evidence to the photothermocatalytic synergetic effect, we measured the catalytic activity of MnO_x/TNS-C for benzene oxidation in a flow fixed quartz tube reactor in dark or with the irradiation of the Xe lamp at the different temperature (Experimental). As shown in Fig. 11, at the same reaction temperature above 160 °C, the photothermocatalytic $r_{CO_2\text{-ptc}}$ of MnO_x/TNS-C with the irradiation of the Xe lamp is higher than the corresponding thermocatalytic $r_{CO_2\text{-tc}}$ in dark. The $r_{CO_2\text{-ptc}}$ of MnO_x/TNS-C with the irradiation of the lamp at 160, 180, 200, 220, 240, 260 °C is 9.6, 18.1, 32.9, 63.3, 127.7, 221 μmol g^{-1} min^{-1}, respectively. The $r_{CO_2\text{-ptc}}$ is 1.4, 1.7, 1.6, 2.0, 1.8, 1.5 times higher than the corresponding summation of the thermocatalytic $r_{CO_2\text{-tc}}$ at the same reaction temperature in dark and the photocatalytic $r_{CO_2\text{-pc}}$ at ambient temperature, respectively. The results clearly reveal that the highly efficient activity of the MnO_x/TNS-C nanocomposite under the full solar spectrum irradiation (Fig. 6) originates from the photothermocatalytic synergetic effect between the photocatalysis on anatase TiO_2 nanosheet and the solar light-driven thermocatalysis on amorphous manganese oxide.

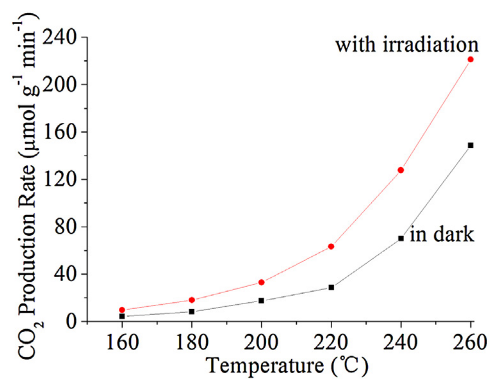

Fig. 11. CO_2 production rate for benzene oxidation of the MnO_x/TNS-C sample in dark and with the irradiation of the Xe lamp at the different temperature under the condition of benzene concentration = 2.0 g m^{-3}, space velocity (SV) = 96000 mL $g_{catalyst}^{-1}$ h^{-1}.

3.4.1. *Origin of Synergetic Effect*

As discussed above, the solar light driven thermocatalysis, mainly occurred on amorphous manganese oxide for the MnO_x/TNS-C nanocomposite, follows Mars–van Krevelen mechanism. It is well known that the reducibility of manganese oxide plays a decisive role in its thermocatalytic activity because the reduction of manganese oxide is more sluggish than the re-oxidation of reduced manganese oxide [51,52,62]. To put more insight in the photothermocatalytic synergetic effect, we investigated the effect of the solar light irradiation on the reducibility of the MnO_x/TNS-C nanocomposite by CO temperature-programmed reduction (CO-TPR) in dark and with the irradiation of the Xe lamp (Experimental). Under the condition in dark, there is a strong CO consumption peak in the region of 140–300 °C, which is attributed to the reduction of amorphous manganese oxide in the MnO_x/TNS-C nanocomposite by CO. In addition, there is a negative peak around 60 °C, which is attributed to the desorption of CO absorbed on the MnO_x/TNS-C nanocomposite. Very interestingly, compared to the CO-TPR in dark, the full solar spectrum irradiation of the Xe lamp

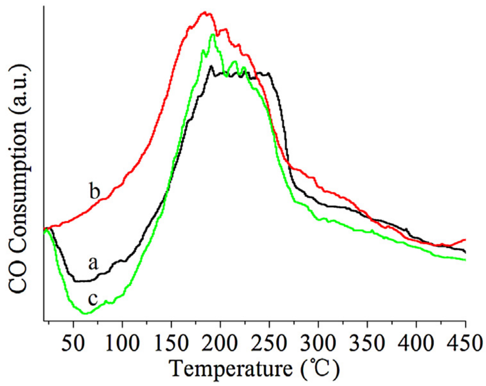

Fig. 12. CO-TPR of MnO_x/TNS-F-C in dark condition (a), under the full solar spectrum irradiation of the Xe lamp (b), and under the visible-infrared irradiation above 480 nm (c).

leads to a considerable shift of the CO consumption peak to lower temperature. The CO consumption peak shift to lower temperature may arise from the following reason: the photogenerated holes in TiO_2 nanosheets in the MnO_x/TNS-C nanocomposite upon full solar spectrum irradiation leads to the formation of O^- species from lattice O^{2-} ions ($h^+ + O^{2-} = O^-$) [63].The active O^- species may react with CO, thus resulting in the CO consumption peak shift to lower temperature. But our recent work by

in-situ CO-FTIR reveals that only when the temperature increase above 240 °C, CO can react with the lattice oxygen in TiO_2 nanosheets with exposed {001} to form CO_2, and the UV irradiation can promote the reaction of CO with the lattice oxygen in TiO_2 nanosheets [45]. However, as shown in Fig. 12, CO starts to be consumed when the temperature increases above ~125 °C in dark, and CO starts to be consumed only when the temperature increases above ~30 °C under the full solar spectrum irradiation. The result and discussion clearly indicate that the full solar spectrum irradiation considerably promotes the reduction of amorphous manganese oxide in the MnO_x/TNS-C nanocomposite. Under the condition in dark, there is only the reduction of amorphous manganese oxide by CO. However, under the full solar spectrum irradiation, the photogenerated hole and electron are produced in anatase TiO_2 nanosheet due to the excitation of the UV light from the Xe lamp. The photogenerated hole reacts with CO adsorbed on anatase TiO_2 nanosheet to form active carbon monooxide (CO^+) because of its higher redox potential (3.02 V vs NHE) than that of CO (CO^+/CO, 0.64 V vs NHE) [47,64]. The active carbon monooxide (CO^+) is more active than CO according to molecular orbital theory as the number of electrons in the binding molecular orbital of CO^+ is less than that of CO.[54] The active carbon monooxide (CO^+) migrates from TiO_2 to amorphous manganese oxide through the interface of MnO_x/TiO_2, thus accelerating the reduction of amorphous manganese oxide. To confirm the conclusion, we measured the CO-TPR of the MnO_x/TNS-C nanocomposite under the visible-infrared irradiation above 480 nm. In this case, anatase TiO_2 nanosheet could not be excited due to its large band gap. No active carbon monooxide (CO^+) can be formed by photocatalysis, thus amorphous manganese oxide is reduced only by CO as the case in dark. As expected, compared to the CO-TPR profile in dark, there is no obvious shift of the CO consumption peak to lower temperature under the visible-infrared irradiation above 480 nm.

4. Conclusion

In summary, the nanocomposites of amorphous manganese oxide supported on anatase TiO_2 nanosheet with dominant {001} facets (MnO_x/TNS) with different Mn/Ti molar ratio were prepared by hydrothermal redox reaction of $KMnO_4$ and $Mn(NO_3)_2$ in the presence of anatase TiO_2 nanosheet with dominant {001} facet. The MnO_x/TNS nanocomposite with the optimum Mn/Ti molar ratio of 0.4 exhibits highly efficient photothermocatalytic activity and excellent durability for benzene oxidation under the irradiation of full solar spectrum or visible-infrared light, even with infrared irradiation. The highly efficient photothermocatalytic activity of the MnO_x/TNS nanocomposite under the full solar spectrum irradiation originates from the highly efficient solar light-driven thermocatalysis on the amorphous manganese oxide due to its strong absorption in entire solar spectrum region and the efficient thermocatalytic activity. Moreover, the highly efficient solar light-driven thermocatalysis is considerably promoted by a photothermocatalytic synergetic effect: the active species generated by photocatalysis on TiO_2 nanosheet migrate to amorphous manganese oxide via the MnO_x/TiO_2 interface, and accelerate the solar light-driven thermocatalysis on amorphous manganese oxide. The present work provides an efficient strategy of significantly enhancing photocatalytic activity of anatase TiO_2 nanosheet with dominant {001} facets and efficiently extending its catalytic response from UV to whole solar spectrum region by forming a MnO_x/TNS nanocomposite. The strategy and novel nanostructured materials are expected to have potential application in the environmental abatement using renewable solar energy.

Acknowledgement

This work was supported by National Natural Science Foundation of China (21473127, 21273169).

Appendix A. Supplementary data

Supplementary data associated with this article can be found, in the online version, at http://dx.doi.org/10.1016/j.apcatb.2016.10.047.

References

[1] H.G. Yang, C.H. Sun, S.Z. Qiao, J. Zou, G. Liu, S.C. Smith, H.M. Cheng, G.Q. Lu, Nature 453 (2008) 638–642.
[2] X.G. Han, Q. Kuang, M.S. Jin, Z.X. Xie, L. Zheng, J. Am. Chem. Soc. 131 (2009) 3152–3153.
[3] T.R. Gordon, M. Cargnello, T. Paik, F. Mangolini, R.T. Weber, P. Fornasiero, C.B. Murray, J. Am. Chem. Soc. 134 (2012) 6751–6761.
[4] Z.F. Bian, J. Zhu, J. Wen, F.L. Cao, Y.N. Huo, X.F. Qian, Y. Cao, M.Q. Shen, H.X. Li, Y.F. Lu, Angew. Chem. Int. Ed. 123 (2011) 1137–1140.
[5] C.H. Wang, X.T. Zhang, Y.C. Liu, Nanoscale 6 (2014) 5329–5337.
[6] T.C. An, J.Y. Chen, X. Nie, G.Y. Li, H.M. Zhang, X.L. Liu, H.J. Zhao, ACS Appl. Mater. Interfaces 4 (2012) 5988–5996.
[7] G. Liu, H.G. Yang, J. Pan, Y.Q. Yang, G.Q. Lu, H.M. Cheng, Chem. Rev. 114 (2014) 9559–9612.
[8] X.Y. Pan, N. Zhang, X.Z. Fu, Y.J. Xu, Appl. Catal. A 453 (2013) 181–187.
[9] Q. Shang, X. Tan, T. Yu, Z.Y. Zhang, Y.L. Zou, S.Y. Wang, J. Colloid Interfaces Sci. 455 (2015) 134–144.
[10] Z.K. Zheng, B.B. Huang, J.B. Lu, X.Y. Qin, X.Y. Zhang, Y. Da, Chem. Eur. J. 17 (2011) 15032–15038.
[11] J.G. Yu, J.X. Low, W. Xiao, P. Zhou, M. Jaroniec, J. Am Chem. Soc. 136 (2014) 8839–8842.
[12] N. Roy, Y. Sohn, D. Pradhan, ACS Nano 7 (2013) 2532–2540.
[13] T. Tachikawa, S. Yamashita, T. Majima, J. Am Chem. Soc. 133 (2011) 7197–7204.
[14] X.C. Ma, Y. Dai, M. Guo, B.B. Huang, Langmuir 29 (2013) 13647–13654.
[15] J. Zhu, S.H. Wang, Z.F. Bian, So H. Xie, C.L. Cai, J.G. Wang, H.G. Yang, H.X. Li, CrystEngComm 12 (2010) 2219–2224.
[16] C. Liu, X.G. Han, S.F. Xie, Q. Kuang, X. Wang, M.S. Jin, Z.X. Xie, L.S. Zheng, Chem. Asian J. 8 (2013) 282–289.
[17] M. Maisano, M.V. Dozzi, M. Coduri, L. Artiglia, G. Granozzi, E. Selli, ACS Appl. Mater. Interfaces 8 (2016) 9745–9754.
[18] Z.F. Bian, T. Tachikawa, T. Majima, J. Phys. Chem. Lett. 3 (2012) 1422–1427.
[19] J. Xu, F. Teng, C.Y. Xu, Y. Yang, L.M. Yang, Y.D. Kan, J. Phys. Chem. C 119 (2015) 13011–13020.
[20] G. Liu, H.G. Yang, X.W. Wang, L.N. Cheng, H.F. Lu, L.Z. Wang, G.Q. Lu, H.M. Cheng, J. Phys. Chem. C 113 (2009) 21784–21788.
[21] W. Wang, Y.R. Ni, C.H. Lu, Z.Z. Xu, RSC Adv. 2 (2012) 8286–8288.

[22] Q.J. Xiang, K.L. Lv, J.G. Yu, Appl. Catal. B 96 (2010) 557–564.
[23] Y.B. Luan, L.Q. Jing, Y. Xie, X.J. Sun, Y.J. Feng, H.G. Fu, ACS Catal. 3 (2013) 1378–1385.
[24] B.J. Jiang, C.G. Tian, Q.J. Pan, Z. Jiang, J.Q. Wang, W.S. Yan, H.G. Fu, J. Phys. Chem. C 115 (2011) 23718–23725.
[25] W.S. Wang, D.H. Wang, W.G. Qu, L.Q. Lu, A.W. Xu, J. Phys. Chem. C 116 (2012) 19893–19901.
[26] L. Sun, Z.L. Zhao, Y.C. Zhou, L. Liu, Nanoscale 4 (2012) 613–620.
[27] L.A. Gu, J.Y. Wang, H. Cheng, Y.Z. Zhao, L.F. Liu, X.J. Han, ACS Appl. Mater. Interfaces 5 (2013) 3085–3093.
[28] Y.J. Yuan, Z.J. Ye, H.W. Lu, B. Hu, Y.H. Li, D.Q. Chen, J.S. Zhong, Z.T. Yu, Z.G. Zou, ACS Catal. 6 (2016) 532–541.
[29] C. Peng, X.F. Yang, Y.H. Li, H. Yu, H.J. Wang, F. Peng, ACS Appl. Mater. Interfaces 8 (2016) 6051–6060.
[30] M. Zhang, R.Z. Sun, Y.J. Li, Q.M. Shi, L.H. Xie, J.S. Chen, X.H. Xu, H.X. Shi, W.R. Zhao, J. Phys. Chem. C 120 (2016) 10746–10756.
[31] G. Liu, H.G. Yang, X.W. Wang, L.N. Cheng, J. Pan, G.Q. Lu, H.M. Cheng, J. Am. Chem. Soc. 131 (2009) 12868–12869.
[32] Q.J. Xiang, J.G. Yu, W.G. Wang, M. Jaroniec, Chem. Commun. 47 (2011) 6906–6908.
[33] J.G. Yu, G.P. Dai, Q.J. Xiang, M. Jaroniec, J. Mater. Chem. 21 (2011) 1049–1057.
[34] X. Zong, Z. Xing, H. Yu, Z.G. Chen, F.Q. Tang, J. Zou, G.Q. Lu, L.Z. Wang, Chem. Commun. 47 (2011) 11742–11744.
[35] M.Y. Xing, D.Y. Qi, J.L. Zhang, F. Chen, Chem. Eur. J. 17 (2011) 11432–11436.
[36] L.F. Qi, J.G. Yu, M. Jaroniec, Phys. Chem. Chem. Phys. 13 (2011) 8915–8923.
[37] J.G. Hou, C. Yang, Z. Wang, S.Q. Jiao, H.M. Zhu, Appl. Catal. B 129 (2013) 333–341.
[38] P. Wang, X. Li, J.L. Fang, D.Z. Li, J. Chen, X.Y. Zhang, Y. Shao, Y.H. He, Appl. Catal. B 181 (2016) 838–847.
[39] L.Y. Chen, X.S. Zhou, B. Jin, J. Luo, X.Y. Xu, L.L. Zhang, Y.P. Hong, Int. J. Hydrogen Energy 41 (2016) 7292–7300.
[40] S.Y. Zhu, S.J. Liang, Q. Gu, L.Y. Xie, J.X. Wang, Z.X. Ding, P. Liu, Appl. Catal. B 119 (2012) 146–155.
[41] W.Y. Jiang, S. Bai, L.M. Wang, X.J. Wang, L. Yang, Y.R. Li, D. Liu, X.N. Wang, Z.Q. Li, J. Jiang, Y.J. Xiong, Small 12 (2016) 1640–1648.
[42] L. Ren, Y.Z. Li, J.T. Hou, J.L. Bai, M.Y. Mao, M. Zeng, X.J. Zhao, Appl. Catal. B 181 (2016) 625–634.
[43] B.I. Stefanov, G.A. Niklasson, C.G. Granqvist, L. Österlund, J. Catal. 335 (2016) 187–196.
[44] M.J. Wang, F. Zhang, X.D. Zhu, Z.M. Qi, B. Hong, J.J. Ding, J. Bao, S. Sun, C. Gao, Langmuir 31 (2015) 1730–1736.
[45] L. Ren, M.Y. Mao, Y.Z. Li, L. Lan, Z. Zhang, X.J. Zhao, Appl. Catal. B 198 (2016) 303–310.
[46] J.T. Hou, Y.Z. Li, M.Y. Mao, Y.Z. Yue, G.N. Greaves, X.J. Zhao, Nanoscale 7 (2015) 2633–2640.
[47] M. Zeng, Y.Z. Li, M.Y. Mao, J.L. Bai, L. Ren, Z.J. Zhao, ACS Catal. 5 (2015) 3278–3286.
[48] F. Liu, M. Zeng, Y.Z. Li, Y. Yang, M.Y. Mao, X.J. Zhao, Adv. Funct. Mater. 26 (2016) 4518–4526.
[49] M.Y. Mao, Y.Z. Li, J.T. Hou, M. Zeng, X.J. Zhao, Appl. Catal. B 174 (2015) 496–503.
[50] Y. Ma, Y.Z. Li, M.Y. Mao, J.T. Hou, M. Zeng, X.J. Zhao, J. Mater Chem. A 3 (2015) 5509–5516.
[51] J.T. Hou, Y.Z. Li, L.L. Liu, L. Ren, X.J. Zhao, J. Mater, Chem. A 1 (2013) 6736–6741.
[52] J.T. Hou, L.L. Liu, Y.Z. Li, M.Y. Mao, H.Q. Lv, X.J. Zhao, Environ. Sci. Technol. 47 (2013) 13730–13736.
[53] S.F. Jin, Y.Z. Li, H. Xie, X. Chen, T.T. Tian, X.J. Zhao, J. Mater, Chem 22 (2012) 1469–1476.
[54] G.D. Zhou, Y.L. Duan, The Basis of Structural Chemistry, Peking University Press, Peking China, 2008, pp. 1–363.
[55] A.L. Linsebigler, G.Q. Lu, J.T. Yates, Chem. Rev. 95 (1995) 735–758.
[56] X.B. Chen, S.S. Mao, Chem. Rev 107 (2007) 2891–2959.
[57] M. Kong, Y.Z. Li, X. Chen, T.T. Tian, P.F. Fang, F. Zheng, X.J. Zhao, J. Am. Chem. Soc. 133 (2011) 16414–16417.
[58] Y.L. Zheng, W.Z. Wang, D. Jiang, L. Zhang, X.M. Li, Z. Wang, J. Mater. Chem. A 4 (2016) 105–112.
[59] T. Tachikawa, M. Fujitsuka, T. Majima, J. Phys. Chem. C 111 (2007) 5259–5275.
[60] O. d'Hennezel, P. Pichat, D.F. Ollis, J. Photochem. Photobiol. A 118 (1998) 197–204.
[61] D.T. Sawyer, J.S. Valentine, Acc. Chem. Res. 14 (1981) 393–400.
[62] V.P. Santos, M.F.R. Pereira, J.J.M. Orfao, J.L. Figueiredo, Appl. Catal. B 99 (2010) 353–363.
[63] T. Berger, M. Sterrer, O. Diwald, E. Knozinger, D. Panayotov, T.L. Thompson, J.T. Yates, Jr, J. Phys. Chem. B 109 (2005) 6061–6068.
[64] R. Ianniello, V.M. Schmidt, U. Stimming, J. Super, A. Wallau, Electrochim. Acta 39 (1994) 1863–1869.